



0264-8172(95)00037-2

# Diagenesis of an 'overmature' gas reservoir: the Spiro sand of the Arkoma Basin, USA

**Christoph Spötl\****Institut für Geologie und Paläontologie, Universität Innsbruck, Innrain 52,  
6020 Innsbruck, Austria***David W. Houseknecht***US Geological Survey, 915 National Center, Reston, VA 22092, USA***Stephen J. Burns***Geologisches Institut, Universität Bern, Baltzerstrasse 1, 3012 Bern, Switzerland**Received 12 January 1995; revised 6 March 1995; accepted 29 March 1995*

The Spiro sand is a laterally extensive thin sandstone of earliest Atokan (Pennsylvanian) age that forms a major natural gas reservoir in the western Arkoma Basin, Oklahoma. Petrographic analysis reveals a variety of diagenetic alterations, the majority of which occurred during moderate to deep burial. Early diagenetic processes include calcite cementation and the formation of Fe-clay mineral peloids and coatings around quartz framework grains. These clays, which underwent transformation to well-crystallized chamosite [polytype  $Ib(\beta = 90^\circ)$ ] on burial, are particularly abundant in medium-grained channel sandstones, whereas illitic clays are predominant in fine-grained interchannel sandstones. Subsequent to mechanical compaction, saddle ankerite precipitated in the reservoir at temperatures in excess of 70°C. Crude oil collected in favourable structural locations during and after ankeritization. Whereas hydrocarbons apparently halted inorganic diagenesis in oil-saturated zones, cementation continued in the underlying water-saturated zones. As reservoir temperatures increased further, hydrocarbons were cracked and a solid pyrobitumen residue remained in the reservoir. At temperatures exceeding ~140–150°C, non-syntaxial quartz cement, ferroan calcite and traces of dickite(?) locally reduced the reservoir quality. Local secondary porosity was created by carbonate cement dissolution. This alteration post-dated hydrocarbon emplacement and is probably related to late-stage infiltration of freshwater along 'leaky' faults. The study shows that the Spiro sandstone locally retained excellent porosities despite deep burial and thermal conditions that correspond to the zone of incipient very low grade metamorphism.

**Keywords:** diagenesis; gas reservoirs; Arkoma Basin, Oklahoma

Our present understanding of diagenetic processes in sedimentary rocks is to a great extent the result of research stimulated by the search for hydrocarbons. As known petroleum resources are being depleted, strategies are directed increasingly towards the exploration of natural gas occurrences in the deeper and hotter portions of sedimentary basins.

One of the frontier areas of deep basin gas exploration in the USA is the Arkoma Basin and the adjacent Ouachita thrust belt. The Arkoma Basin is a prolific natural gas province, despite thermal maturity levels that are considered 'overmature' (Houseknecht and Spötl, 1993). Here, we focus on reservoir diagenesis of the Spiro sandstone (informal industry term widely applied to a quartzose sandstone at the base of the Pennsylvanian Atoka Formation; Branan, 1968), in the Oklahoma portion of the Arkoma basin (*Figure 1*). Although this sandstone underwent deep burial to

conditions approaching very low grade metamorphism (Houseknecht and Spötl, 1993), it locally retained excellent porosity and permeability and is a prolific natural gas reservoir. Our objectives are to document the diagenetic history of the Spiro sandstone and to constrain the physical and chemical conditions under which diagenesis occurred.

## Geological setting

The Arkoma Basin is one of a number of foreland basins that formed in response to the late Palaeozoic Ouachita orogeny (Houseknecht, 1986). The stratigraphic succession in the Arkoma Basin is marked by two distinct phases of sedimentation: (1) from Late Cambrian to Early Pennsylvanian (late Morrowan) shallow water carbonates, siliciclastics and chert were deposited on the stable, gently southward dipping margin of the North American craton; (2) during the Middle Pennsylvanian (and perhaps to Late Pennsylva-

\* Correspondence to Dr C. Spötl

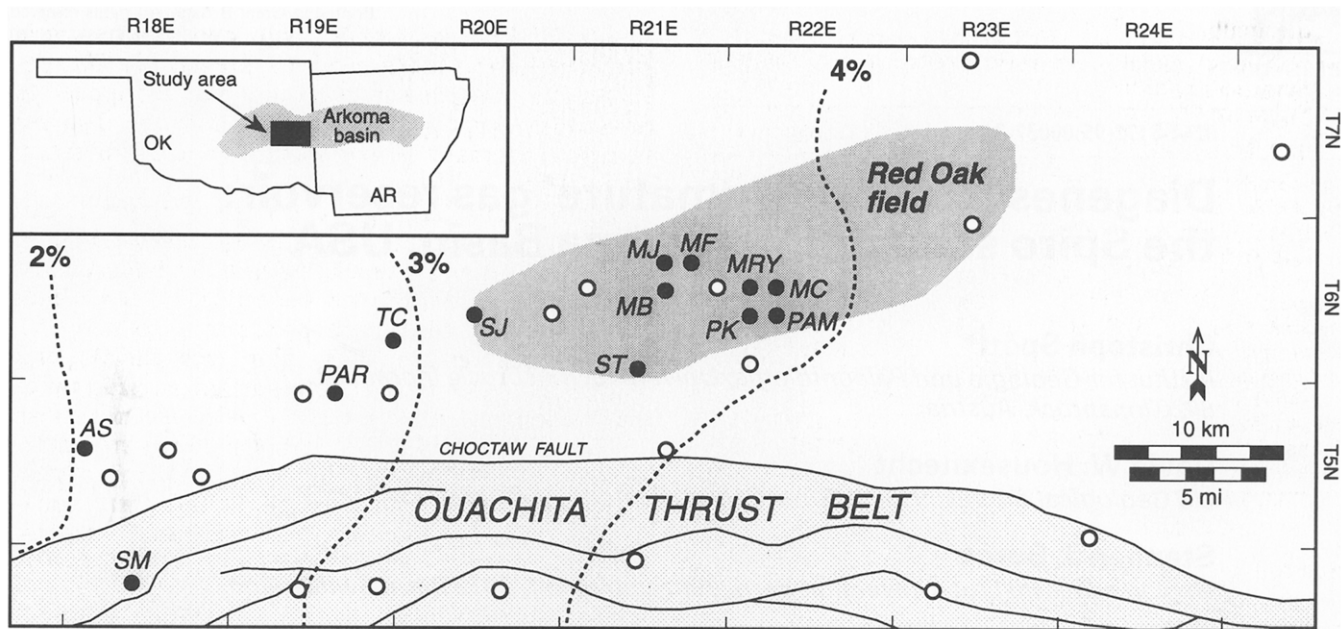


**Figure 1** Map showing locations of wells studied within the Red Oak field and adjacent areas in the southern part of the Arkoma Basin, immediately north of the frontal Ouachita thrusts. All circles indicate wells studied for thermal maturity (vitrinite reflectance), except PAM; closed circles indicate wells studied for Spiro sandstone mineral diagenesis. For well abbreviations, see Table 1. The dotted lines are isoreflectance contours at the Spiro sandstone level at 2, 3 and 4% rotational reflectance (from Houseknecht and Spötl, 1993). In well SM, Spiro sandstone was studied in the subthrust position

nian or Permian) an episode of foreland basin deposition included the initial rapid accumulation of a wedge of syn-orogenic, mud-rich sediments and, later, of deltaic, fluvial and coal-bearing strata that together reach thicknesses of up to 6.5 km. The Spiro sand is a 12–60 m thick sandstone of earliest Atokan age that was deposited immediately before the downwarping of the shelf and the subsequent onset of flysch sedimentation (Figure 2).

This study is based primarily on Spiro sandstone samples from the Red Oak gas field in eastern Oklahoma, located immediately north of the Ouachita frontal thrust belt and adjacent areas (Figure 1 and Table 1). Subsurface mapping of the Spiro sandstone at the Red Oak field revealed several NW–SE trending channels cutting into finer grained interchannel sediments (Lumsden *et al.*, 1971; Houseknecht and McGilvery, 1990). Facies reconstructions suggest a broad, tidally swept, sandy coastal environment incised by fluvially dominated channels grading southward into open marine shelf environments dominated by carbonate mudstones (Houseknecht, 1986).

The Arkoma Basin in general and the Red Oak field in particular are examples of commercial natural gas production from high thermal maturity strata. Vitrinite reflectance of the Spiro increases from ~2% to more than 4% eastward across the study area (Figure 1) and may indicate maximum burial temperatures on the order of ~190–250°C (using the empirical relationship of Barker and Pawlewicz, 1994). This lateral thermal maturity gradient is typical of strata throughout the study area, including near-surface coal beds, whose vitrinite reflectance values increase eastward from less than 1.0 to about 1.5% across the Red Oak field (Houseknecht *et al.*, 1992).

## Methods

This study is based on petrographic and geochemical analyses of 170 samples collected from conventional drill cores (Table 1). Samples were examined both in thin section and as broken chips by scanning

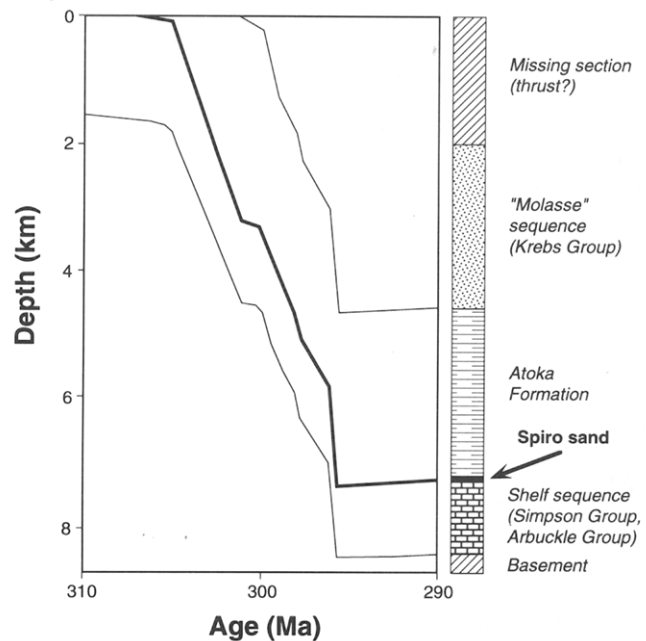


**Figure 2** Simplified compaction-corrected subsidence curves for the AD well located to the east of the Red Oak field (see Figure 1 for location), illustrating the rapid subsidence of the Arkoma Basin during the interval 310–290 Ma (Late Pennsylvanian). The Spiro sandstone is highlighted underlying flysch of the Atoka Formation

**Table 1** List of wells from which samples were analysed. *N* is the number of samples examined from each well. For well locations, see Figure 1

Well	Code	State	Township	<i>N</i>
Ambassador Smith	AS	OK	20-5N-18E	20
Pan Am Reusch	PAR	OK	3-5N-19E	4
Shell Jankowsky	SJ	OK	21-6N-20E	4
Sarkeys Thrift	ST	OK	33-6N-21E	14
Midwest Booth	MB	OK	15-6N-21E	19
Midwest Jones	MJ	OK	10-6N-21E	15
Midwest Free	MF	OK	11-6N-21E	38
Midwest Coblenz	MC	OK	16-6N-22E	10
Midwest Rider	MRY	OK	17-6N-22E	13
Pan Am Kent	PK	OK	19-6N-22E	4
Pan Am Martin	PAM	OK	20-6N-22E	11
Tenneco Kraft	TC	OK	25-6N-19E	12
Shell Mabry	SM	OK	9-4N-18E	9

electron microscopy (SEM) with an X-ray analytical system. Thin sections were cut from blue dye epoxy-impregnated blocks to facilitate porosity identification. Carbonate cements were studied by cathodoluminescence (CL) and back-scattered electron (BSE) imaging using a scanning electron microscope. A commercial cold-cathode luminescope was used for petrography and operated at ~20 kV beam potential, 500–600 mA beam current and ~7 Pa pressure. Subsequently, the elemental composition of individual carbonate cements was determined using an electron microprobe operating at 15 kV accelerating voltage and 50 nA sample current. Most analyses were performed using a 10 µm beam diameter, but very small crystals were probed using either a 5 or 1 µm diameter beam. Natural calcite, dolomite, siderite and strontianite were used as standards. Counting times of 30 s for Ca, Mg, Fe, Mn and Sr were used (all elements measured wavelength-dispersively). Raw data were reduced using the Bence-Albee method. On the basis of counting statistics the detection limits for CaO, MgO, FeO, MnO and SrO are approximately 0.02, 0.02, 0.05, 0.05 and 0.03 wt. %, respectively. The elemental composition of chlorite cements was determined by electron microprobe analysis on polished thin sections (analytical details given in Spötl *et al.*, 1994).

Based on detailed petrographic analysis, samples containing only a single carbonate cement phase were selected for stable isotope analysis. Ankerite containing calcite was purified by reaction in 30% acetic acid at room temperature. Sample purity was confirmed by powder X-ray diffraction (XRD) analysis. We also analysed the stable isotopic composition of individual crinoid stem fragments embedded in black, argillaceous mudstones (sampled using a dental drill device). Calcites were reacted on-line with 100% phosphoric acid at 90°C and ankerites were dissolved off-line at 50°C overnight. Mass spectrometric measurements were performed at the University of Berne. Isotopic ratios are quoted relative to PDB. The reproducibility is better than 0.1‰ for  $\delta^{13}\text{C}$  and better than 0.2‰ for  $\delta^{18}\text{O}$ . No correction was applied to account for the differential fractionation of ankerite (relative to calcite) dissolving in phosphoric acid.

Fluid inclusion microthermometric measurements were performed using a USGS-type gas-flow heating–cooling stage calibrated against known melting point

standards. For carbonates, only one heating cycle per sample was performed to prevent *in situ* re-equilibration. A pressure correction was not applied to homogenization temperatures; therefore the data are minimum estimates of entrapment or re-equilibration temperature.

Vitrinite reflectance measurements were performed on dispersed vitrinite particles concentrated from Atoka Formation mudrocks using a newly developed technique that allows the collection of reflectance data while the microscope polarizer is rotated 360° (Houseknecht *et al.*, 1993). For each sample, this method yields several variables, including mean maximum reflectance, mean rotational reflectance and mean minimum reflectance. The thermal maturity parameter used in this study is the mean rotational reflectance, which is essentially equivalent to the reflectance parameter commonly used in many dispersed organic studies ( $R_o$  or  $R_{\text{ran}}$ ; Houseknecht *et al.*, 1993).

### Detrital sandstone composition

The Spiro sandstone in the Red Oak field is a fine-to medium-grained, texturally and compositionally mature quartz arenite. Medium-grained sandstones commonly retaining high porosities (typically 10–18%) characterize fluvial channel-fills, whereas interchannel sandstones are finer grained and of lower porosity (<5%). Data presented in this study are mostly from medium-grained channel sandstones.

Mono- and polycrystalline quartz varieties (including chert) commonly comprise >95 vol. % of the framework grains; the remainder being green particles (see later) and rare sedimentary rock fragments. Bioclasts are locally abundant and include crinoid ossicles, echinoid spines, bryozoan fragments and brachiopod and bivalve shells. The former presence of small amounts of chemically unstable framework grains may be deduced only from the local occurrence of moulds; no feldspar is present in the Spiro of Red Oak field today. Illitic matrix clays are confined to the finer grained interchannel sandstones.

Brown to greenish chamosite (Fe-rich, trioctahedral chlorite) ooids and peloids are common in many channel-fill samples. Some of these particles are optically homogeneous, whereas others consist of a core enveloped by concentric laminae. Inclusions of detrital quartz grains and authigenic apatite are commonly present in these particles. Some samples contain abundant chamosite matrix. Transitions between chlorite coats and diffuse intergranular chlorite matrix are common. Electron microprobe analyses show that both have identical elemental compositions. Additional information about chlorite in the Spiro sandstone is provided in Spötl *et al.* (1994).

### Diagenetic events

This section focuses on the diagenetic history of the medium-grained sandstones because of their significance as natural gas reservoir rocks; this represents a detailed refinement of the general diagenetic history described by Houseknecht (1987a), who also provided a general discussion of the diagenesis of non-productive, finer grained interchannel sandstone facies. A

general paragenetic sequence is shown in *Figure 3*. Unfortunately, the Spiro sandstone lacks cements suitable for isotopic age dating, so the inferred paragenesis is relative and no absolute time connotations beyond that of early and late are used. The timing of inorganic diagenesis relative to hydrocarbon emplacement, however, is well constrained in this reservoir because solid hydrocarbons (pyrobitumen) are present in some cores and are post-dated by later stage cements.

#### Compaction features

Direct evidence for mechanical compaction is confined to deformation of ductile chamosite peloids and matrix, and bending of rare detrital muscovite. However, it is assumed that the brittle components (mostly quartz grains) underwent rotation and repacking during shallow burial because the observed intergranular volumes are indicative of sands that have been mechanically compacted (e.g. Houseknecht, 1987b). Grain breakage is uncommon, primarily because of the small amounts of low strength, brittle components, such as certain rock fragments and feldspar grains.

Despite deep burial, the channel facies of the Spiro sandstone shows little evidence of chemical compaction. Grain contacts are mostly of the long and concave-convex types, but point contacts are also present. Intergranular pressure solution was apparently inhibited, probably by some combination of factors that included the common presence of chlorite coatings on framework grains, overpressured conditions and the presence of hydrocarbons.

Finer grained sandstones and coarse siltstones of the interchannel facies as well as channel-fill sandstones pervasively cemented by early diagenetic carbonate commonly show low amplitude (<5 mm) stylolite seams. Higher amplitude (>1 cm) stylolites were observed locally along boundaries of porous chloritic

sandstones and tightly cemented, ankeritic sandstones of the channel facies.

#### Sandstone cements

Carbonate, chlorite and quartz are the volumetrically most significant cements in medium-grained facies of the Spiro sandstone. Minor cements include apatite, sulphides and dickite(?). Authigenic feldspar, illite and evaporitic minerals, common in other deep burial settings, are absent in the Spiro sandstone.

**Chlorite.** One of the most obvious features of porous, semi-friable channel sandstones is the abundance of green chlorite enveloping detrital framework grains. The thickness of the coatings ranges mostly from 15 to 25 µm. Electron microprobe and XRD studies reveal a high Fe composition (chamosite, Spötl *et al.*, 1994). Chlorite rims commonly extend between the contacts of individual grains. XRD and SEM investigations reveal that most chloritic samples are composed of two generations of grain-rimming chlorite showing distinct structural states and slightly different elemental compositions (Spötl *et al.*, 1994), an earlier chlorite of the Ib ( $\beta = 90^\circ$ ) polytype and a late chlorite generation that is structurally IIb. The relative abundance of polytype IIb gradually increases with increasing thermal maturity (Spötl *et al.*, 1994). Textural observations suggest that precipitation of chlorite IIb post-dated major compaction, but pre-dated quartz cementation and overlaps pyrobitumen formation.

**Rhodochrosite.** Mn-carbonate crystals (10–30 µm) were identified in a few samples by using BSE microscopy. These crystals are aligned along the boundaries of framework grains and are overgrown by later stage ankerite. Rhodochrosite cores are non-luminescent and BSE examination reveals that they consist of numerous submicron-sized crystals. The mean chemical composition of the rhodochrosite is

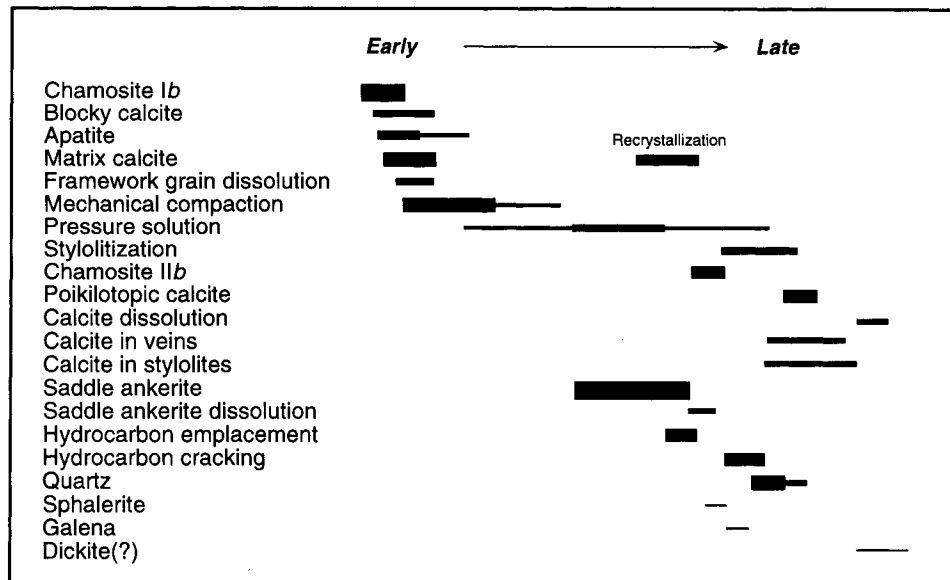


**Figure 3** Summary chart of diagenetic alterations in the Spiro sandstone. The two petrographic varieties of quartz are not distinguished here and the bar shown on this chart is representative of mainly 'quartz B' (see text for further explanation). Pressure solution is an important process in the finer grained interchannel sand- and siltstones, but is minor in the medium-grained channel sandstones. The volumetric significance of individual diagenetic processes is indicated by the relative thickness of the bars

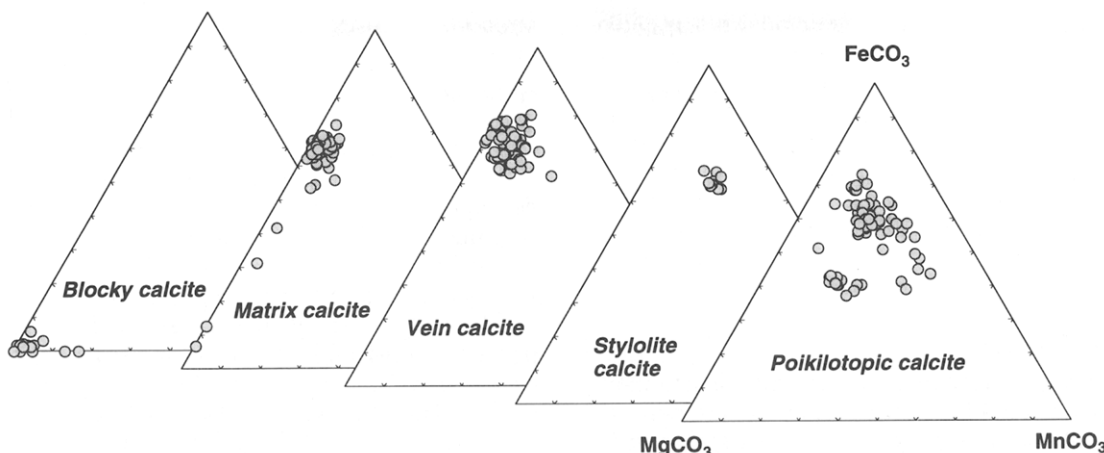


**Figure 4** Comparison of relative minor and trace element compositions of various diagenetic calcites in the Spiro sandstone. With the exception of early blocky calcite, all other cements show a tendency towards ferroan compositions

$\text{Ca}_{0.31}\text{Mg}_{0.08}\text{Fe}_{0.03}\text{Mn}_{0.58}\text{CO}_3$  (Sr concentrations below detection limit; mean of  $n = 9$  analyses). Micritic rhodochrosite also occurs in carbonate peloids, intergrown with non-ferroan calcite.

**Apatite.** A fairly common, though minor, diagenetic constituent is apatite. Apatite is commonly overlooked during standard petrographic work because of its small crystal size (10–40  $\mu\text{m}$ ) and overall optical similarity with quartz. Using CL, however, apatite is readily identified by its bright bluish white colour. Apatite appears texturally early, is highly replacive against detrital quartz and is commonly found in leached chloritic and phosphatic peloids.

**Blocky calcite.** Medium- to fine-grained sandstones rich in bioclasts are commonly cemented by blocky calcite crystals that nucleated on echinoderm fragments and form syntaxial overgrowths. The overgrowths eventually coalesced and occluded all intergranular porosity. Most blocky calcite crystals are non-luminescent, but thin, dull brown to moderately bright orange luminescent zones define local CL growth patterns. Fe, Mn and Sr concentrations for this non-luminescent calcite are mostly below the detection limit for the electron microprobe. The average Mg concentration is  $1.8 \pm 0.5$  mole %  $\text{MgCO}_3$  ( $n = 18$ ), i.e. low Mg calcite (Figure 4). Three samples yielded fairly low oxygen isotope ratios ( $-9.2$  to  $-7.8\text{\textperthousand}$  PDB) and carbon isotope values between  $-1.5$  and  $+0.4\text{\textperthousand}$  PDB (Figure 5).

We also studied the petrography and geochemical composition of crinoid ossicles from one well (SM) in an attempt to constrain the composition of the early pore water. Petrographic analysis reveals that the crinoid fragments show a variable degree of preservation. The original stereome structure is mostly well preserved and readily seen in normal transmitted light. The initial high Mg calcite is replaced by a moderately bright orange luminescent low Mg calcite (1.5 mole %  $\text{MgCO}_3$ ,  $<0.3$  mole %  $\text{FeCO}_3$ ), in which anhedral to subhedral microdolomite inclusions (5–15  $\mu\text{m}$ ) are common. Microprobe analyses indicate a calcian dolomite composition,  $\text{Ca}_{0.530}\text{Mg}_{0.468}\text{Fe}_{0.002}\text{CO}_3$  (Mn and Sr concentrations below detection limit). Dully luminescent, mildly ferroan calcite ( $1.6 \pm 0.2$  mole %  $\text{MgCO}_3$ ,  $1.2 \pm 0.2$  mole %  $\text{FeCO}_3$ ,  $0.09 \pm 0.08$  mole %

$\text{MnCO}_3$   $0.09 \pm 0.02$  mole %  $\text{SrCO}_3$ ;  $n = 10$ ) commonly fills the central lumen of crinoids. BSE imaging reveals traces of authigenic barite, pyrite and celestite within the moderately bright orange luminescent calcite. Silicification is also common in some samples. The stable isotope composition of individual crinoid ossicles is shown in Figure 5.

**Matrix calcite.** Ferroan calcite is a common early diagenetic cement that occupies moderate to high intergranular volumes and pre-dates burial cements (Figure 3). Matrix calcite is particularly abundant in cores cut near the channel margins as well as within the finer grained interchannel sandstones. Syntaxial calcite overgrowths on echinoderm fragments and authigenic apatite locally pre-date matrix calcite cementation. Matrix calcite consists of poorly defined crystals, showing irregular grain boundaries and patchy and faintly undulose extinction. Electron microprobe analyses of five samples ( $n = 47$  point analyses) show that the matrix calcite contains  $1.5 \pm 0.5$  mole %  $\text{MgCO}_3$ ,  $2.9 \pm 1.0$  mole %  $\text{FeCO}_3$ ,  $0.2 \pm 0.09$  mole %  $\text{MnCO}_3$  and  $0.09 \pm 0.04$  mole %  $\text{SrCO}_3$  (Figure 4). Matrix calcite reveals moderately bright orange-red

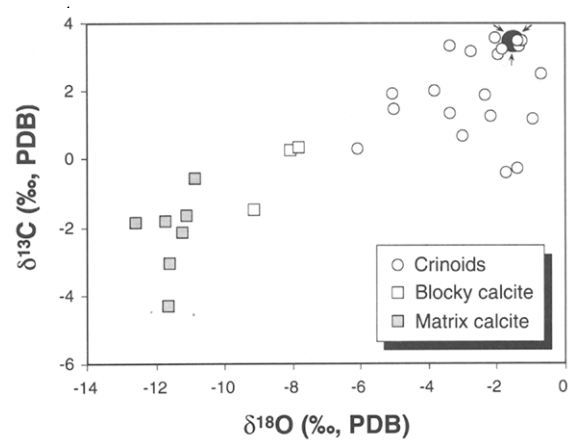


**Figure 5** Stable isotope composition of texturally early carbonate cements and crinoid ossicles from the Spiro sandstone. The black dot and the arrows indicate the approximate composition of abiogenic calcite precipitated from Atokan seawater (taken from Lohmann and Walker, 1989)

CL despite high Fe concentrations (*Plate 1B*). Oxygen isotope ratios of matrix calcite range from  $-12.6$  to  $-10.9\text{‰}$  PDB and carbon isotope ratios range from  $-4.3$  to  $-0.6\text{‰}$  PDB ( $n = 7$ ; *Figure 5*).

**Saddle ankerite.** Ankeritic dolomite of characteristic saddle-shaped habit is a very common cement in the Spiro sand. Ankerite primarily replaces framework

grains and earlier formed cements (e.g. matrix calcite) and has a turbid appearance in transmitted light due to numerous solid inclusions of possibly organic origin. Some saddle ankerite crystals enclose small, irregularly shaped pyrobitumen particles along their outer crystal rims. Ankerite is volumetrically insignificant in porous channel sandstones that have well-developed chlorite

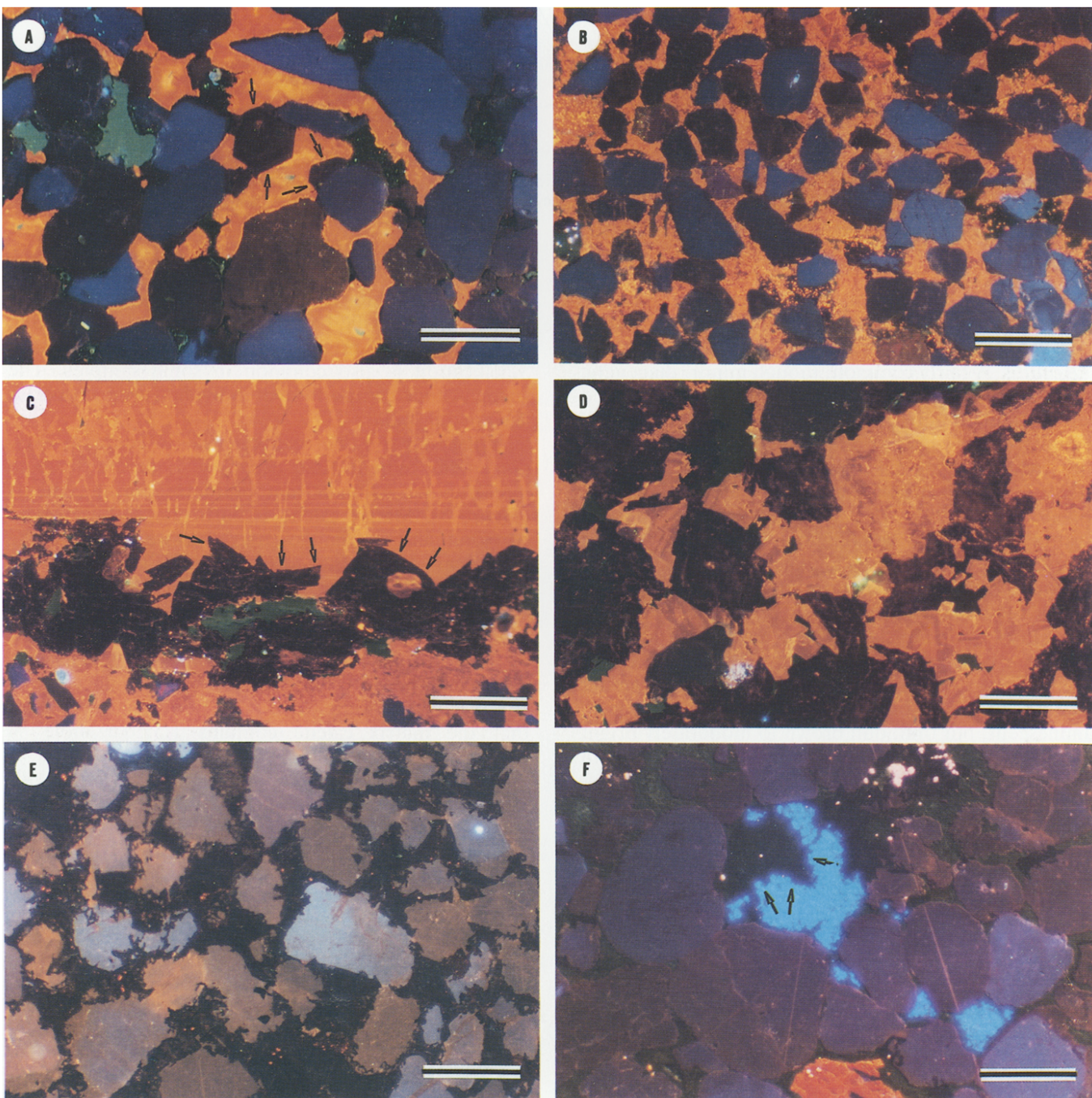


**Plate 1** Petrographic characteristics of carbonate cements in the Spiro sandstone as seen under CL. All scale bars are  $250\text{ }\mu\text{m}$  (A). Poikilotopic calcite (orange) post-dating quartz cement (arrows). Note long contacts between quartz framework grains, suggesting that significant mechanical and chemical compaction occurred before calcite precipitation. Porosity is green. (B) Typical appearance of a sandstone cemented by matrix calcite. Note inhomogeneous and patchy CL patterns, particular in the upper half of the photomicrograph. (C) Non-luminescent ankerite lining the wall of a fracture that is cemented by bright yellow luminescent calcite (upper half of photomicrograph). Note curved, saddle-shaped crystal outline of some of the larger crystals (arrows). The fracture cut through matrix calcite-cemented sandstone (bottom). (D) Replacement of dark brown saddle ankerite by poikilotopic calcite along a thin fracture. Dark green areas are porosity (epoxy). (E) Sandstone entirely cemented by non-luminescent saddle ankerite. Note marginal replacement of detrital quartz grains by ankerite crystals. The brownish pink CL colour of quartz is due to long exposure under the electron beam. (F) Brightly blue luminescent, pore-filling dickite(?) engulfing corroded ankerite (arrows). Surrounding grains are quartz. Yellow luminescent crystal at the bottom of the photomicrograph is calcite and white specks are authigenic apatite crystals

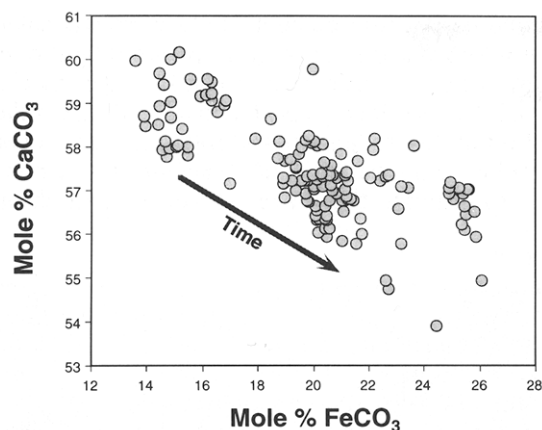


**Figure 6** Elemental composition of saddle ankerite as determined by electron microprobe analysis of 11 samples. The arrow indicates the inferred general trend towards higher Fe substitution and less Ca excess with increasing time

rims. In contrast, finer grained sandstones of the interchannel facies, but also some samples from chlorite-poor channel sandstones, show higher amounts of diagenetic ankerite. Locally, ankerite also is present in fractures, post-dated by calcite. Electron microprobe analyses of saddle ankerites show excess Ca (mean =  $57.4 \pm 1.1$  mol. %  $\text{CaCO}_3$ ;  $n = 1.35$ ), the amount of which is inversely proportional to the Fe concentration (Figure 6). Saddle ankerite is entirely non-luminescent under CL (Plate 1C, 1D and 1E). BSE imaging shows

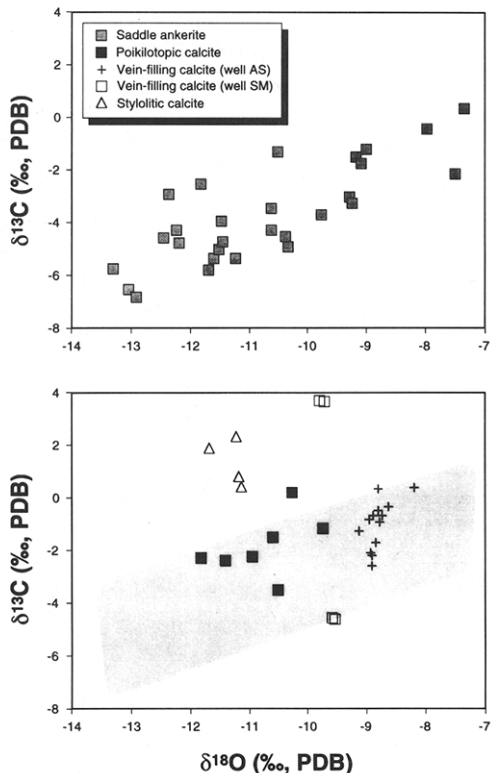


**Figure 7** Stable isotope composition of burial carbonate cements in the Spiro sandstone. The upper diagram shows the range in carbon and oxygen isotope ratios of saddle ankerites. Values for burial calcite cements are plotted on the lower diagram. The grey array indicates the compositional range of saddle ankerites

that most ankerite crystals are compositionally homogeneous, although some crystals show Fe-enriched rims as well as complex intergrowths of compositionally distinct zones similar to those described by Wojcik *et al.* (1992). Saddle ankerite displays a range in stable isotope composition with all values significantly depleted in  $^{18}\text{O}$  (Figure 7). The data points define a linear trend of decreasing oxygen isotope ratios with decreasing carbon isotope ratios. Attempts to locate fluid inclusions suitable for microthermometric analysis in these ankerites were unsuccessful.

**Pyrobitumen.** An opaque carbonaceous residue is present in many cores of the Spiro sandstone from the Red Oak field (Plate 2). Textural observations show that hydrocarbon emplacement occurred largely subsequent to widespread saddle ankerite cementation in the reservoir and was possibly accompanied by local ankerite dissolution. There might also have been some overlap of these processes, as suggested by the occurrence of hydrocarbon particles in the outer portion of ankerite crystals. Porous samples from the dead oil zone commonly show hydrocarbon impregnated chlorite coatings. Interestingly, only the outer zone of these rims is stained by pyrobitumen, whereas the inner layer (10–15  $\mu\text{m}$  wide) remained unstained (cf. Spötl *et al.*, 1994).

**Quartz.** Authigenic quartz is a common and locally abundant burial cement in channel facies of the Spiro sandstone. Two petrographic types of quartz can be distinguished. (1) 'Quartz A' forms syntaxial overgrowths on detrital sand grains of the interchannel facies; these overgrowths are typically thin and difficult to distinguish from the detrital cores because of the absence of chlorite coats in these sandstones. The resultant texture resembles that of a quartzite with curved grain boundaries meeting at  $\sim 120^\circ$  junctions and very low porosities. Importantly, CL microscopy reveals that the intergranular volume (IGV) of sandstones cemented by quartz A is fairly low and that moderate pressure solution has affected the sediment before quartz cementation. (2) Sandstones from the channel facies, characterized by chlorite coatings and high IGVs, show locally extensive quartz cementation whose petrographic appearance differs markedly from quartz A. Unlike syntaxial quartz, 'quartz B' forms

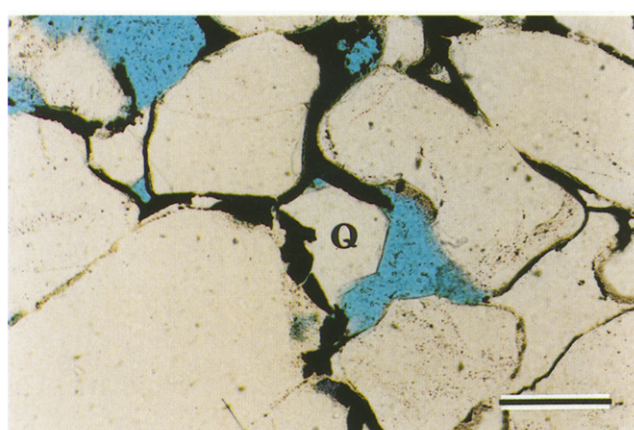


**Plate 2** Residual pyrobitumen (black) in a Spiro sandstone sample, post-dated by late-stage quartz cement (Q). Plane light photomicrograph. Scale bar 100  $\mu\text{m}$

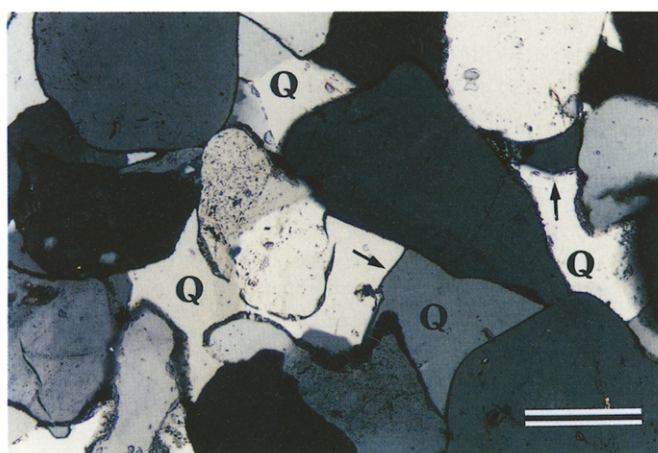


**Plate 3** Quartz arenite of the Spiro sandstone completely cemented by late-stage quartz (Q). Note that this type of quartz cement does not form syntaxial overgrowths on the detrital grains. Individual authigenic quartz crystals are bound by curved compromise boundaries (arrows). Crossed polars. Scale bar 200 µm

coarsely crystalline crystal aggregates that nucleated on quartz grains where the chlorite coating was incomplete (Pittman and Lumsden, 1968) and produced protrusions into the open pore space. These crystals engulf portions of several adjacent framework grains and eventually coalesce to form an exceptionally clear and inclusion-free quartz cement occluding most porosity (Plate 3). Only minor pressure solution pre-dated quartz B precipitation in these samples. Under CL, this pseudo-poikilotopic quartz reveals complex growth patterns composed of alternating dull green, blue and thin non-luminescent zones. Sector zoning is particularly common. The faint emission colours are short-lived (cf. Ramseyer and Mullis, 1990) and change to homogeneous medium brown after electron bombardment of ~10–20 s. The damage is permanent and occurs more readily in green luminescent than in blue luminescent zones. In contrast, detrital quartz retains its indigenous emission colours significantly longer (usually 1–2 minutes under the operating conditions described under Methods) before changing to the brown damage-induced colour. Quartz B is commonly

associated with pyrobitumen. Petrographic observations show that quartz B largely post-dates pyrobitumen formation (Plate 2), as indicated by quartz crystals filling bubble cavities and shrinkage cracks of the pyrobitumen (Houseknecht and McGilvery, 1990; their figures 10 and 11). Minor quartz B, however, also predates pyrobitumen in some samples. Quartz B is most abundant immediately beneath hydrocarbon-impregnated sandstones.

Quartz cement is also present in stylolites. Stylolitic quartz crystals are up to several hundred micrometres in length, essentially unstrained and post-dated by calcite. Textural observations, including the close association of vein stylolite quartz and pyrobitumen and the engulfing of quartz by a late-stage calcite cement, suggest that this type of quartz cement might be largely coeval with the formation of quartz B in other samples. A minor silica variety in some stylolites is microcrystalline, chert-like quartz.

Although no fluid inclusion was found in quartz A and B, a few small ( $\leq 5 \mu\text{m}$ ) two-phase aqueous inclusions are present in euhedral stylolitic quartz. These inclusions are concentrated in the outer portion of the quartz crystals and appear primary in origin. Most inclusions contain a small, vibrating vapour bubble that occupies between 20 and 30% of the inclusion volume. All inclusions homogenize into the liquid phase and total homogenization temperatures range from 154 to 218°C (mean =  $193 \pm 21^\circ$ ; Figure 8). The melting of the final ice was difficult to observe and all  $T_{\text{m}_{\text{ice}}}$  values are  $-3.2^\circ\text{C}$  or higher. One-third of the inclusions showed  $T_{\text{m}_{\text{ice}}}$  as high as  $+14^\circ\text{C}$ , suggesting the presence of clathrates of carbon dioxide and methane (Figure 8). Determination of the salinity of such complex systems requires precise knowledge of additional clathrate phase changes (Collins, 1979), which could not be determined due to the small size of the inclusions.

*Poikilotopic calcite.* A late-stage, brightly orange luminescent calcite cement is locally present in channel facies of the Spiro sandstone. It is distributed in patches and some samples show evidence of leaching (e.g. in well ST). Poikilotopic calcite post-dates thermal cracking of oil and quartz cementation (Plate 1A) and may replace saddle ankerite (Plate 1D). Electron microprobe analyses of seven samples indicate a

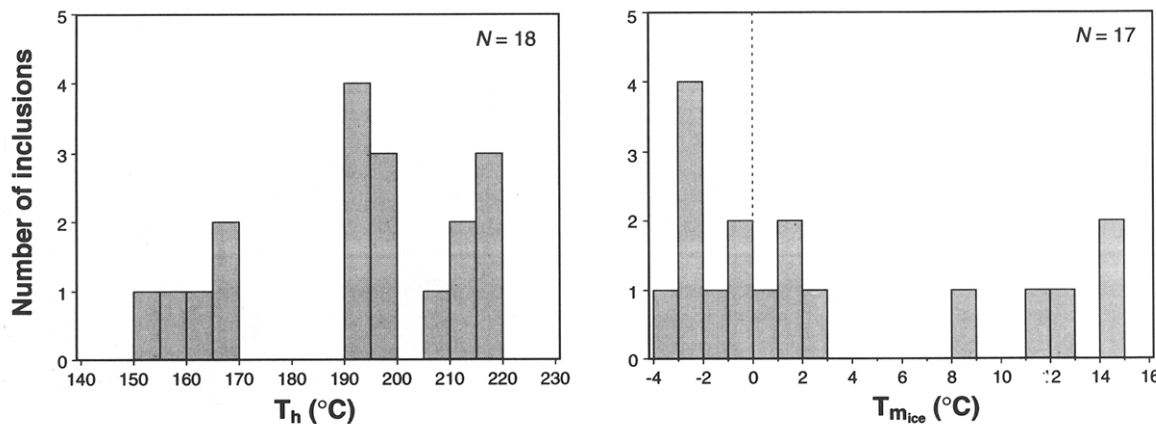


**Figure 8** Homogenization temperatures ( $T_h$ ) and last ice melting temperatures ( $T_{\text{m}_{\text{ice}}}$ ) of fluid inclusions in quartz crystals growing along stylolites. Note high  $T_{\text{m}_{\text{ice}}}$  values indicative of clathrate formation

ferroan composition:  $1.0 \pm 0.6$  mole %  $\text{MgCO}_3$ ,  $2.1 \pm 0.5$  mole %  $\text{FeCO}_3$ ,  $0.8 \pm 0.4$  mole %  $\text{MnCO}_3$  and  $0.1 \pm 0.1$  mole %  $\text{SrCO}_3$  ( $n = 78$ ; Figure 4). Carbon isotope ratios range from  $-3.5$  to  $+0.2\text{\textperthousand}$  PDB and oxygen isotope values range from  $-11.8$  to  $-9.8\text{\textperthousand}$  PDB ( $n = 7$ ; Figure 7).

**Calcite in veins and stylolites.** Calcite cemented fractures, up to about 2 cm in width, are common in well AS (Table 1) and are important because this calcite contains fluid inclusions suitable for microthermometry. Vein-filling calcite shows homogeneous, bright orange CL and post-dates saddle ankerite along fracture walls (Plate 1C). The chemical composition of five samples ( $n = 65$ ) is only slightly different from the composition of poikilotopic calcite:  $0.5 \pm 0.2$  mole %  $\text{MgCO}_3$ ,  $1.7 \pm 0.3$  mole %  $\text{FeCO}_3$ ,  $0.2 \pm 0.1$  mole %  $\text{MnCO}_3$  (Figure 4); Sr concentrations are mostly near or below detection limit.  $\delta^{13}\text{C}$  and  $\delta^{18}\text{O}$  ratios of vein-filling calcite from the AS well range from  $-2.6$  to  $+0.4\text{\textperthousand}$  PDB and from  $-9.1$  to  $-8.2\text{\textperthousand}$  PDB, respectively (Figure 7). Thin tectonic fractures filled by milky calcite are also present in well SM (Table 1), which was drilled into Spiro rocks present in a subthrust position. We sampled two different generations of these fracture-filling calcites and obtained different carbon isotopic compositions. The first type has heavier  $\delta^{13}\text{C}$  values ( $+3.7\text{\textperthousand}$ ) relative to the second type, which has lighter  $\delta^{13}\text{C}$  values ( $-4.6\text{\textperthousand}$ ).  $\delta^{18}\text{O}$  values are almost identical ( $-9.6$  and  $-9.8\text{\textperthousand}$ ; two samples analysed each; Figure 7).

Two-phase, liquid-rich aqueous inclusions are common in vein-filling calcite. The measured inclusions mostly range from 3 to 8  $\mu\text{m}$  and a few inclusions are up to 12  $\mu\text{m}$  in diameter. Inclusions are either highly elongate and/or show irregular outlines. Few of the inclusions measured meet all the criteria for primary inclusions (Roedder, 1984) and many inclusions show evidence of stretching and leakage, including spine-like extensions (cf. Prezbindowski and Tapp, 1991). In addition, secondary inclusions formed by necking down along healed microfissures are common (not measured). No daughter crystal was observed in any inclusion. The vapour bubble is usually stable at room temperature. With one exception, all inclusions homogenized in the liquid phase. Homogenization was mostly well observed (within  $\pm 0.5^\circ\text{C}$ ), unless the bubble was hidden in a re-entrant of the inclusion.

Forty-two fluid inclusions were heated and homogenized to determine  $T_h$ , which ranges from  $143$  to  $253^\circ\text{C}$  with a mean of  $181 \pm 22^\circ\text{C}$  (Figure 9). Sixty-two inclusions were frozen and then warmed to determine the temperature of the eutectic ( $T_e$ ) and the temperature of the melting of the final ice ( $T_{\text{mice}}$ ).  $T_e$  was not observed and active melting of the ice was recognized in only a few larger and thicker inclusions. In these instances, unequivocal melting was observed only a few degrees centigrade below  $T_{\text{mice}}$ . The final ice melting temperature was marked by the sudden reappearance of the vapour bubble, occasionally followed by slow bubble movement as the last ice crystals were melting.  $T_{\text{mice}}$  values range from  $-3.0$  to  $+0.9^\circ\text{C}$ , with most values being slightly lower than  $0^\circ\text{C}$  (mean  $-1.2 \pm 0.8^\circ\text{C}$ ; Figure 9). Salinity estimates based on the pure  $\text{H}_2\text{O}-\text{NaCl}$  system yields  $\leq 5$  wt. %  $\text{NaCl}$  eq.

We also studied calcite cement occurring in stylolites. This calcite apparently grew during stylolitization, as indicated by extremely long and thin, semi-fibrous crystals aligned parallel to the stylolite and the presence of kinked twin lamellae. Based on cross-cutting relationships, stylolitic calcite (and hence the stylolitization process) post-dated ankeritization as well as quartz cementation of the Spiro. Stylolitic calcite displays bright orange CL, similar to the emission colour observed in vein-filling calcite. Microprobe analyses of one sample ( $n = 12$ ) suggest a similar elemental composition to the vein-filling variety:  $0.6 \pm 0.1$  mole %  $\text{MgCO}_3$ ,  $2.5 \pm 0.2$  mole %  $\text{FeCO}_3$ ,  $0.7 \pm 0.1$  mole %  $\text{MnCO}_3$  and  $0.1 \pm 0.02$  mole %  $\text{SrCO}_3$  (Figure 4).  $\delta^{13}\text{C}$  values are positive ( $+0.4$  to  $+2.3\text{\textperthousand}$ ) and  $\delta^{18}\text{O}$  values are uniformly negative ( $-11.7$  to  $-11.1\text{\textperthousand}$ ; Figure 7).

**Dickite(?)**. Cathodoluminescence microscopy revealed the presence of traces of a kaolin mineral showing moderately bright blue luminescence. This cement is confined to individual pores (Plate 1F) and was only detected in a few samples. It is clearly a late diagenetic phase, post-dating ankerite, quartz and poikilotopic calcite. Because dickite is a common late-stage diagenetic product in sandstones higher in section within the Atoka Formation (i.e. Red Oak sandstone; Houseknecht and Ross, 1992), we tentatively identify this clay mineral in the Spiro as the high temperature polymorph dickite. An isotope analysis of a single dickite sample from the Red Oak sandstone in Red Oak field yielded a  $\delta^{18}\text{O}$  ratio of  $+16.1\text{\textperthousand}$  SMOW

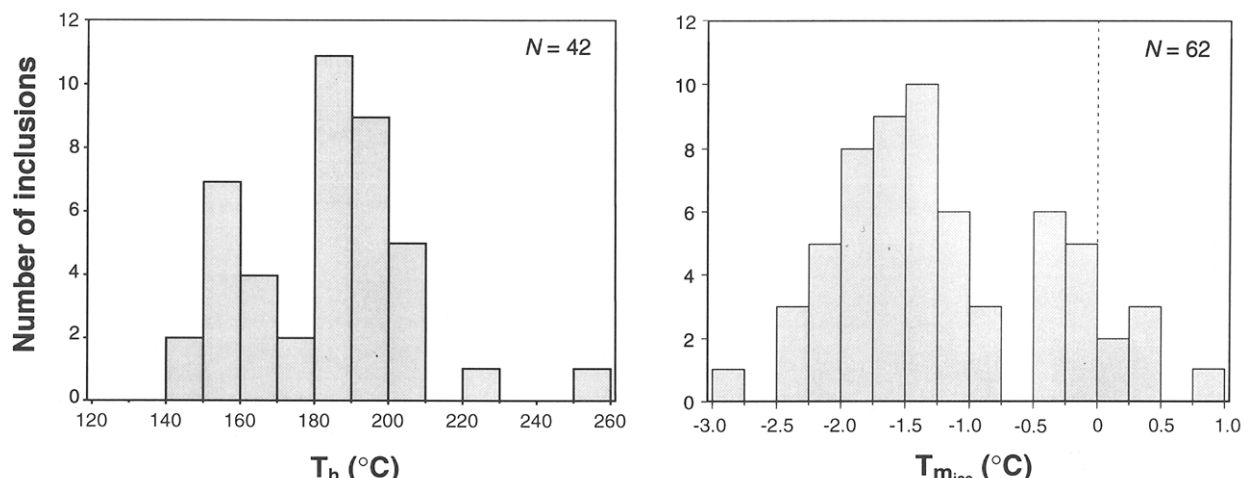


Figure 9 Homogenization temperatures ( $T_h$ ) and last ice melting temperatures ( $T_{\text{mice}}$ ) of fluid inclusions in calcite fractures

(analyst Dr F. J. Longstaffe).

**Sulphides.** Traces of ~10 µm sized frambooidal pyrite aggregates composed of ~1 µm crystallites were identified in both ankerite and matrix calcite, suggesting earlier growth. Late-stage sphalerite and galena occur in some stylolites.

#### Porosity types

The bulk of the porosity in channel facies of the Spiro sandstone is intergranular and appears to be preserved primary porosity. Primary porosity preservation is clearly related to the presence of chlorite coats.

There is clear evidence of an early diagenetic event of framework grain dissolution, as indicated by leached chlorite peloids and bioclasts and rare mouldic porosity filled partly by apatite and carbonate cements. In addition, locally significant secondary porosity also was generated by the dissolution of saddle ankerite and poikilotopic calcite (e.g. in well ST). However, evidence of a widespread pervasive cement-dissolution event affecting the early calcite cements (e.g. matrix calcite) is lacking.

Minor microporosity is present within chlorite cements, as indicated by their blue epoxy stain in thin section. Core analyses show that fracture porosity is locally significant and few fractures are cemented by calcite (e.g. well AS).

Measured total porosity in the Spiro sandstone ranges from 1 to 24%, and permeabilities between about tens and several hundred millidarcy have been reported from the main reservoir units (Houseknecht and McGilvery, 1990).

## Discussion

### Early diagenesis

Early diagenetic processes, i.e. reactions that occurred before substantial mechanical compaction of the sand, are difficult to reconstruct because later events modified many of their products. Examples include the abundant chlorite rims that were probably formed as either berthierine (a serpentine mineral) or some sort of 'swelling chlorite', and matrix calcite whose isotopic composition implies burial recrystallization (see later).

Crucial for the understanding of early diagenetic processes and hence the destruction or preservation of primary porosity is the question about the type of water involved in these reactions. On the basis of facies reconstructions, the initial water composition in the Spiro sandstone is assumed to be highly variable, ranging from freshwater-dominated to marine (towards the south). Oxygen and carbon isotope ratios depleted relative to the marine composition (Figure 5) as well as the low magnesium contents of early diagenetic blocky calcite suggest a freshwater influence rather than marine conditions during precipitation of the earliest carbonate cements. The presence of marine fossils is not regarded as a reliable indicator of initial pore water chemistry because most of these bioclasts are clearly allochthonous and were probably washed onto the deltaic coast by tidal and/or storm-induced currents. Although carbon and oxygen isotope ratios of crinoid ossicles are largely consistent with an initially marine depositional environment of their formation (Figure 5), the observed diagenetic alteration of high Mg calcite to

low Mg calcite plus (micro)dolomite and minor ferroan calcite, as well as the tendency toward light  $\delta^{18}\text{O}$  and  $\delta^{13}\text{C}$  ratios in some samples (Figure 5), suggest that the early diagenetic environment was freshwater-influenced, if not freshwater-dominated.

Another texturally early cement is matrix calcite. The fairly high intergranular volume occupied by this cement suggests precipitation before major mechanical compaction of the sand. The stable isotope data, however, are difficult to reconcile with this observation. Ratios of  $\delta^{18}\text{O}$  between -12.6 and -10.9‰ PDB would require a highly  $^{18}\text{O}$  depleted pore water (-11.7 to -10.0‰ SMOW at 20°C using Friedman and O'Neil's 1977 equation). Considering the coastal, low latitude setting, such light values are incompatible, even with pure meteoric water. We favour an alternative explanation that also takes into account the rather unusual optical properties of matrix calcite (irregular, patchy crystals, undulose extinction), i.e. burial recrystallization and concomitant isotope resetting. Whether isotopic exchange with the recrystallizing fluid has achieved equilibrium, however, cannot be decided based on these data.

A conspicuous feature of the medium-grained channel facies of the Spiro sandstone is the occurrence of chamosite peloids, matrix and coatings. The peloids clearly formed syn-depositionally, whereas tangential chlorite coats and diffuse chlorite matrix formed soon after deposition. The present day structural state of Spiro chlorites is clearly the result of diagenetic transformation, inasmuch as they are well crystallized 14 Å chlorites [polytype Ib( $\beta = 90^\circ$ ) or IIb] that lack interstratified smectite or serpentine (Spötl *et al.*, 1994). It has been suggested that this chlorite polytype forms by diagenetic alteration of an Fe-clay mineral precursor such as berthierine or 'swelling chlorite' (Curtis *et al.*, 1985; Jahren and Aagaard, 1989; Hillier, 1994). Odin (1988) has identified a variety of possible chlorite precursor phases that are typically very fine crystalline and poorly crystallized (e.g. odinite, phyllite C). Odin (1988; 1990) grouped these minerals into the so-called verdine facies as opposed to the glauconite facies characterized by the formation of glauconite. Fe-clay mineral formation in the verdine facies occurs below the sediment-water interface of a sand-dominated depositional setting. A possible modern analogue for the Spiro chlorites is the verdine facies that has been mapped off the modern Niger delta by Porrenga (1966). There, green clay minerals of the verdine facies occur close to the Niger river mouth in water depths of less than 40 m. The modern tropical setting of the Niger delta is comparable with the low latitude setting of the Arkoma Basin during Spiro sand deposition. Formation of these ferroan silicates requires low  $E_h$  redox conditions in which Fe(II) is readily available. Favourable conditions also require low sulphate concentrations in the pore water, because otherwise pyrite forms due to sulphate reduction. The overall scarcity of pyrite in the Spiro sandstone, coupled with the abundance of reduced iron in the system, indicates that iron (and manganese) reduction processes were more significant than sulphate reduction in these sediments. Apparently, low sulphate concentrations in the early pore waters are consistent with the interpretation of a freshwater-dominated mixing zone

environment. Low  $E_h$  redox conditions are also indicated by the occurrence of early Mn carbonates. Rhodochrosites of similar chemical composition have been reported from modern anoxic marine muds of the brackish Baltic Sea (Jakobsen and Postma, 1989).

#### Burial diagenesis

**The burial thermal regime.** The Spiro sandstone is overlain by a thick pile of turbiditic mudrocks of the Atoka Formation (Figure 2) that accumulated in response to the rapid downwarping of the Ouachita foreland. By the end of the Pennsylvanian the Spiro sandstone was buried beneath about 7 km of foreland flysch and molasse-type sediments (Figure 2). The high ranks of near-surface coal beds in the Arkoma Basin ( $\geq 1\% R_o$ , Houseknecht and Spötl, 1993) indicate that an additional section of either sediments and/or of thrust sheets once rested on top of the presently known basin-fill and was later eroded. Modelling of thermal history suggests that this additional section may have ranged from two to several kilometres thick, depending on the extent to which overpressuring influenced thermal conductivities and advective heat transport affected the thermal maturation of the entire stratigraphic section. Importantly, several lines of evidence indicate that peak thermal maturation post-dated most tectonic deformation in the study area; these include coal beds as young as Missourian (Late Pennsylvanian) that display evidence of this thermal maximum (Hemish, 1988), vitrinite isoreflectance contours that cross-cut major thrust faults (Houseknecht and Spötl, 1993) and vitrinite that displays a predominance of uniaxial optical properties in complexly thrusted areas just south of Red Oak field (Houseknecht and Weesner, 1994). In addition, coal rank studies have demonstrated that the observed thermal maturity pattern was not produced by the present geothermal gradient in the basin (Cardott, 1986). Despite these well-constrained inferences, a comprehensive interpretation of the generally high thermal maturities and especially the pronounced lateral thermal maturity gradients (Figure 10) in the Arkoma Basin has been elusive. Several recent models have evoked differential burial by thrust sheets, advective heat transport and the role of overpressure in modifying thermal conductivities (e.g. Werner and Griffith, 1992; Ge and Garven, 1992; Houseknecht *et al.*, 1992; Cathles, 1993).

The presence of pyrobitumen enables us to distinguish burial cementation that occurred before liquid hydrocarbon emplacement from cementation events that post-date thermal degradation of oil as temperatures further increased in the reservoir.

**Burial carbonate cementation.** The major diagenetic reaction post-dating mechanical compaction and largely pre-dating hydrocarbon emplacement in the Spiro sand is ankerite precipitation. Petrographic and geochemical indices suggest that ankerite precipitation occurred over a range of burial depths and temperatures. Within the Red Oak field, the carbon and oxygen isotope ratios of saddle ankerite vary by as much as 7 and 6‰, respectively, and the Fe content ranges from 13 to 26 mole %  $FeCO_3$  (Figures 6 and 7). Cross-plotting microprobe versus isotope data did not reveal any significant trend. BSE microscopy studies suggest that considerable intrasample and intracrystal inhomogeneity masks the relationship between elemental data (obtained from spot analyses) and isotope ratios (determined from bulk rock samples). BSE and microprobe studies, however, show that, in the case of compositionally zoned crystals, earlier formed saddle ankerite is more calcian and less ferroan than later formed ankerite. On the basis of this observation, the covariance between  $\delta^{18}O$  and  $\delta^{13}C$  ratios (Figure 7) is best explained by burial-induced evolution of the chemical environment of ankerite precipitation. The earlier ankerite is characterized by up to 60 mole %  $CaCO_3$ , moderately high Fe contents (of the order of 15 mole %  $FeCO_3$ ), relatively heavy (up to positive)  $\delta^{13}C$  ratios and  $\delta^{18}O$  ratios between -7 and -8‰. The later ankerite is less calcian, but still non-stoichiometric, highly ferroan (up to 26 mole %  $FeCO_3$ ) and has light carbon and oxygen ratios. We infer that the former represents the relatively shallow burial end-member and the latter the relatively deep burial end-member of a continuum of ankerite chemistry. A decrease in the amount of excess Ca in the ankerite with increasing burial temperature and a concomitant increase in the amount of Fe substitution (Figure 6) have also been observed in other sedimentary basins (Boles, 1978; Kantorowicz, 1985; Land and Fisher, 1987; Dutton and Land, 1988) as well as in modern geothermal systems (McDowell and Paces, 1985).

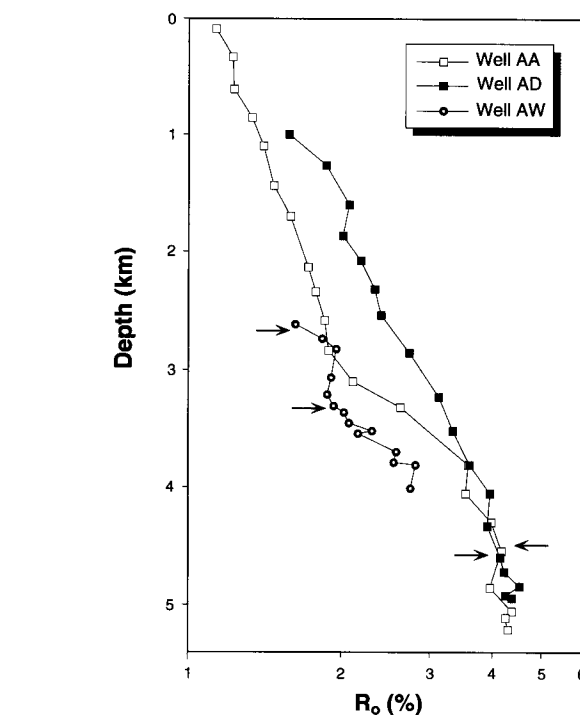


**Figure 10** Vitrinite reflectance ( $R_o$ ) profiles for three wells in the Arkoma Basin (for location of wells, see Figure 1). Arrows indicate the depth of the basal Atoka Formation. Note that the Spiro sandstone was not penetrated in the AA well and the position of the basal Atoka Formation overlying the Spiro is shown by the arrow. In well AW the Spiro sandstone was encountered twice (subthrust and thrusted). Note the similar depth- $R_o$  slope of these profiles.  $R_o$  values plotted on logarithmic scale

Precipitation temperatures of saddle ankerite cannot be constrained directly because no fluid inclusion was found in these poorly translucent crystals. Oxygen isotope data, however, can be used to place constraints

on the minimum temperature of ankerite precipitation in the reservoir. Although the precise  $\delta^{18}\text{O}_{\text{pore water}}$  from which ankerite formed is unknown, it is assumed to be  $\geq -1\text{\textperthousand}$  SMOW (Figure 11), which is the estimated isotopic composition of low latitude Pennsylvanian seawater (Hudson and Anderson, 1989; Lohmann and Walker, 1989). This assumption seems reasonable considering that the Spiro sandstone is immediately overlain by a thick pile of basinal marine mudrocks and interbedded sandy turbidites of the Atoka Formation. Syn-depositional normal faults active during Atoka deposition juxtaposed the marine mudrocks against the Spiro sandstone (Houseknecht, 1986) and provided a direct pathway for pore waters expelled from compacting Atoka muds to exchange with the initial pore waters in the Spiro, probably causing an increase in the  $\delta^{18}\text{O}_{\text{pore water}}$ . This inferred change from freshwater-dominated toward marine conditions in the Spiro pore waters also is consistent with the observed change in carbonate cement mineralogy from low Mg calcite to ferroan dolomite/ankerite, inasmuch as seawater is a plausible source for  $\text{Mg}^{2+}$ . Rock–water interactions in the Spiro sandstone and possibly in juxtaposed Atoka mudrocks (e.g. smectite to illite reaction) may also have contributed to shifting the  $\delta^{18}\text{O}_{\text{pore water}}$  towards positive values, although a complementary study suggests the latter effect may have been minor as a majority of the illite in Atoka mudrocks appears to be of detrital origin (Spötl *et al.*, 1993). Evidence suggesting freshwater input into the burial system is lacking. Using the marine  $-1\text{\textperthousand}$  SMOW value as a starting point, minimum equilibrium precipitation temperatures of  $68\text{--}121^\circ\text{C}$  can be obtained for ankerite in the Spiro sandstone, although values as high as  $200^\circ\text{C}$  appear plausible, if not likely. These temperature estimates are consistent with (1) petrographic observations suggesting ankerite post-dating mechanical compaction and (2) the occurrence

of solid hydrocarbon particles enclosed by ankerite in some samples. The observed correlation of  $\delta^{13}\text{C}$  and  $\delta^{18}\text{O}$  ratios in the ankerite (Figure 7) reflects higher concentrations of isotopically light hydrogencarbonate in the pore water as the temperature increased. This  $^{13}\text{C}$ -depleted hydrogencarbonate could either have been derived from the oil-prone Late Devonian and Early Mississippian Woodford Shale and/or the gas-prone Atoka mudrocks. Maturation (catagenesis) of organic matter into liquid hydrocarbons begins at  $\sim 0.5\% R_o$  (Powell and Snowdon, 1983; Tissot and Welte, 1984), which is close to the estimated minimum temperature of ankerite precipitation in the Red Oak field [ $\sim 80^\circ\text{C}$  using Barker and Pawlewicz's (1994)  $R_o$ -temperature relationship].

Interesting parallels exist between saddle ankerites in the Spiro sandstone and ferroan carbonate cements in strata of equivalent age of the Cherokee Basin of southeastern Kansas, located about 300 km NNW of the Arkoma Basin (Wojcik *et al.*, 1992; 1994). There, saddle ankerite and ferroan dolomite form late-stage burial cements in sandstones and interbedded limestones, respectively. The elemental composition of this saddle ankerite is similar to the early generation of the Spiro ankerites, although they also show considerable compositional variations (Wojcik *et al.*, 1992). Similar to our observations in the Red Oak field, ankerite precipitation in the Cherokee Basin coincided with oil emplacement, as indicated by hydrocarbon inclusions. Aqueous fluid inclusions hosted in the Kansas cements record (pressure-uncorrected) temperatures between  $95$  and  $140^\circ\text{C}$ , which, in conjunction with the oxygen isotope data of the cements, suggest equilibrium  $\delta^{18}\text{O}_{\text{pore water}}$  ratios between  $+3$  and  $+8\text{\textperthousand}$  SMOW (Wojcik *et al.*, 1994). To explain the high temperatures, high salinities (up to 25 wt. % NaCl eq.) and isotopically heavy compositions, Wojcik *et al.* (1994) invoke fluid flow from the Arkoma Basin onto the stable cratonic foreland. If the Spiro ankerites formed from fluids of similar oxygen isotope composition as those in the Cherokee Basin, they would have formed at a temperature range of  $100\text{--}285^\circ\text{C}$ . This range is at least partially consistent with the temperature estimates discussed earlier (cf Figure 11).

Matrix calcite yielded fairly light oxygen isotope ratios, which are difficult to reconcile with an early, pre-compactional origin of this cement. These values, in conjunction with petrographic characteristics (see earlier), suggest calcite recrystallization. The timing of this alteration process is unknown, but petrographic observations showing calcite replaced by saddle ankerite suggest that recrystallization and concomitant isotope resetting of matrix calcite possibly occurred during ankeritization. Equilibrium isotope temperatures, calculated using the same water composition as for ankerite precipitation (i.e.  $\geq -1\text{\textperthousand}$  SMOW) are  $\geq 72\text{--}86^\circ\text{C}$ , which is within the temperature range inferred for saddle ankerite formation (assuming high water–rock ratios).

**Burial silicate cementation.** Quartz cementation is a late diagenetic event in the Spiro reservoir, post-dating chlorite and saddle ankerite precipitation. We observed two petrographic types of secondary quartz whose occurrence appears largely facies-controlled.

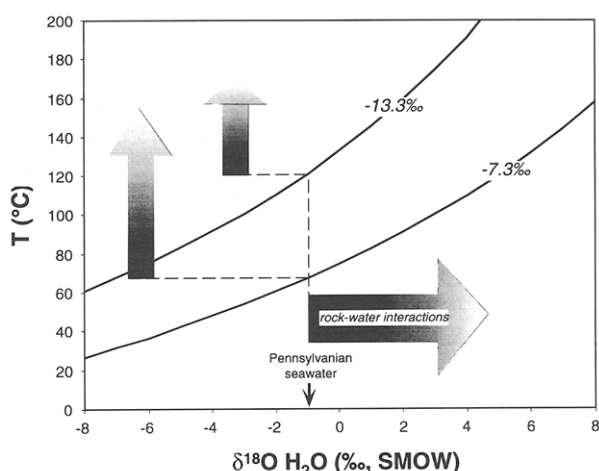


Figure 11 Relationship between  $\delta^{18}\text{O}$  ratio of the saddle ankerite (total range  $-13.3$  to  $-7.3\text{\textperthousand}$  PDB),  $\delta^{18}\text{O}$  of the pore water and equilibrium temperature, using the equation of Fisher and Land (1986). The thick arrow indicates the inferred pore water isotopic composition of the Spiro sandstone during burial ( $\geq -1\text{\textperthousand}$  SMOW) and the thinner arrows show the resulting equilibrium formation temperatures of ankerite cements. Pennsylvanian seawater composition according to Hudson and Anderson (1989) and Lohmann and Walker (1989). For details, see text

Quartz A is uncommon in the main reservoir and produces tightly cemented, low porosity sandstones in the interchannel facies. Quartz B was found in porous reservoir sandstones only. The fundamental difference is the strikingly different IGVs occupied by quartz A and B. We speculate that this difference is the result of several factors. The finer grain size and presence of illitic clays probably promoted chemical compaction in the interchannel facies (e.g. Houseknecht and Hathon, 1987). In contrast, the coarser grain size and presence of chlorite coats and hydrocarbons probably inhibited both chemical compaction and quartz precipitation in the reservoir facies. The fact that quartz B displays a habit that is not commonly observed in quartz cements suggests that its precipitation represented 'conflicting' precipitation conditions. The presence of chlorite grain coats and hydrocarbon residues obviously acted to inhibit quartz cementation by masking nucleation surfaces, but high temperatures probably provided the kinetic impetus to locally overcome those inhibiting factors. Quartz precipitation at sites where grain coats were broken, or where quartz crystals precipitating beneath the grain coats (documented experimentally by Pittman *et al.*, 1992) 'broke through' those coats would result in the observed habit of quartz B. The relative timing of quartz A and B is difficult to establish, mainly because they do not coexist in individual samples. Although some observations suggest that they might actually represent one single diagenetic event (e.g. apparent transitions from syntaxial quartz overgrowths to non-syntaxial quartz B in some samples from well ST), others point towards two distinct episodes of silica precipitation (e.g. contrasting IGVs and textures). There is no doubt, however, that both petrographic quartz types formed during intermediate to deep burial. Because this study focuses on the porous channel sandstones that typically lack the syntaxial variety of quartz cement, we will not discuss its origin further.

**Pyrobitumen.** The origin of the hydrocarbon residue in the Spiro cores has not been studied, but it is believed to be the result of thermal cracking of liquid hydrocarbons. Crude oil migrated into the Spiro sand during intermediate burial and underwent thermal cracking to natural gas and polymerized solid pyrobitumen as reservoir temperatures further increased. Deasphalting (cf. North, 1985) also could have played a significant part during the thermal degradation of the crude oil. A possible source of this crude oil is the oil-prone Late Devonian to Early Mississippian Woodford Shale, which occurs approximately 300 m below the Spiro sandstone and is locally juxtaposed to the Spiro along normal faults.

**Post-hydrocarbon diagenesis.** Locally, inorganic diagenesis continued after liquid hydrocarbon emplacement (*Plate 2*), suggesting that hydrocarbon saturation was low, and/or that flushing of the reservoir by water occurred subsequent to hydrocarbon cracking (cf. Hayes, 1991). Chlorite coats around framework grains record such an example. Samples from palaeo-oil legs commonly show optically zoned chlorite rims, whereby the outer layer is hydrocarbon stained, whereas the inner layer is not. We demonstrate elsewhere (Spötl *et*

*al.*, 1994) that chlorite in this inner, water-saturated layer shows a different crystal habit from chlorite in the hydrocarbon-impregnated layer. The former chlorite is inferred to be of the high temperature IIb polytype, whereas the low temperature Ib structure is preserved in the latter. In other words, although chlorite diagenesis was halted in the outer layer, apparently because of hydrocarbon impregnation, it continued in the inner, water-saturated layer in response to rising burial temperatures. Another interesting aspect of this high temperature diagenesis is the occurrence of a rather unusual type of authigenic silica, i.e. quartz B. This cement occluded the primary porosity in channel sandstones below palaeo oil–water contacts. It also formed locally within the hydrocarbon-saturated zone, as indicated by the presence of quartz filling shrinkage cracks and bubble cavities in pyrobitumen. In the absence of fluid inclusion data, we can only constrain the temperature of formation of quartz indirectly. Three different approaches are used here: (1) authigenic quartz within stylolites that is inferred to be largely equivalent to quartz B yielded homogenization temperatures of two-phase fluid inclusions of 154–218°C; (2) experimental studies suggest that significant thermal cracking of oil requires temperatures on the order of  $\geq 140$ –150°C (Barker, 1990); and (3) quartz B post-dates late-stage chamosite IIb (*Figure 3*), whose occurrence indicates temperatures in excess of  $\sim 140$ –150°C (Spötl *et al.*, 1994). The fluid inclusion data, though preliminary, suggest that the system was complex and involved significant concentrations of dissolved CH<sub>4</sub> and CO<sub>2</sub>. Because the precipitation of quartz largely post-dated the thermal degradation of liquid hydrocarbons, elevated concentrations of these gases logically would have been present in the Spiro reservoir pore water. The inferred quartz precipitation temperatures overlap with the maximum burial temperature of the Spiro in the Red Oak field as estimated from vitrinite reflectance data [ $\sim 2$ –4%  $R_o$ ] (*Figure 1*) corresponding to  $\sim 190$ –250°C using Barker and Pawlewicz's (1994) empirical relationship]. Quartz B precipitation thus probably coincided with peak thermal conditions.

The latest cements to form in the Spiro reservoir are calcite and dickite(?). Although textural observations and electron microprobe data suggest that poikilotopic, vein-filling and stylolitic calcites may be genetically related (*Figure 4*), stable isotope data are difficult to reconcile with this interpretation (*Figure 7*). Note that this picture is clearly biased because of sample availability and the data on vein-filling calcite (all from well AS) may not be representative of the entire study area. A few qualitative constraints, however, can be placed on the formation of fracture-filling calcite in well AS, where both fluid inclusion and isotope data are available. Textural observations document that calcite post-dates ankerite precipitation (*Plate 1C*), therefore temperatures in excess of those expected for ankerite precipitation can be assumed. Two-phase fluid inclusions indeed homogenize at fairly high temperatures (*Figure 9*). Petrographic observations, however, suggest that the majority of the inclusions in vein-filling calcite from well AS may have re-equilibrated as burial temperatures continued to rise. We therefore regard the measured homogenization temperatures as likely to

be too high, in particular the values in excess of 180°C (*Figure 9*). No  $T_h$  measurements are available from wells further east, i.e. from areas of higher thermal maturity. Salinity estimates based on  $T_{m_{ice}}$  values are also fraught with problems because of clathrate formation on heating. Although ice melting in a simple H<sub>2</sub>O–NaCl system at –1°C indicates 1.7 wt. % NaCl eq., clathrate melting in a H<sub>2</sub>O–NaCl–CO<sub>2</sub> system at –1°C indicates about 16.5 wt. % NaCl eq. (Collins, 1979). The addition of CH<sub>4</sub> and other gases will shift the melting point towards even higher temperatures. Because the exact composition of the inclusion could not be determined, we regard the salinity estimates (based on  $T_{m_{ice}}$ ) as likely to be too low. Oxygen isotope values from a number of fracture-filling calcite samples from well AS define a narrow range from –9.1 to –8.2‰ PDB. Assuming equilibrium precipitation, these values, in conjunction with precipitation temperatures well above those assumed for ankerite, suggest heavy  $\delta^{18}\text{O}_{\text{pure water}}$  ratios (e.g. +8.7 to +9.6‰ SMOW at 150°C). Similar compositions are indicated by oxygen isotope values of authigenic chlorite in the Spiro (Spötl *et al.*, 1994). Such <sup>18</sup>O-enriched pore water ratios are common in deep burial settings, in particular where shales are abundant (e.g. Schecki and Land, 1983; Wilkinson *et al.*, 1992).

No fluid inclusion data is available for poikilotopic calcite, but by comparison with fracture-filling calcite, the lower oxygen isotope ratios suggest precipitation at higher temperatures (assuming similar pore water compositions). This interpretation is consistent with the occurrence of poikilotopic calcite in wells to the east of well AS, in areas of higher thermal maturity (*Figure 1*).

There is strong petrographic evidence for a locally significant dissolution event post-dating poikilotopic calcite precipitation. Carbonate dissolution is particularly abundant in well ST, resulting in 'floating grain' textures. Drilling reports show that this particular well penetrated wet Spiro and produced 'freshwater'. Unfortunately, no chemical analyses of this pore water are available, nor did we have access to water samples. It therefore can only be speculated that meteoric water locally infiltrated into the Spiro along faults and caused late-stage (telogenetic) secondary dissolution porosity. This porosity, however, is economically unimportant because its formation apparently post-dated hydrocarbon emplacement. Note, however, that only a small fraction of all wells drilled in the study area have penetrated wet Spiro. The majority of Spiro penetrations either encountered porous, gas-bearing sandstone or non-porous sandstone.

### Implications for deeply buried reservoirs

As the search for hydrocarbons, particularly natural gas, is expanded into the deeper parts of sedimentary basins and thrust belts, the potential for the preservation of reservoir quality becomes an increasingly important consideration. In fact, the concept of depth and/or thermal maturity controlled 'deadlines' for economic reservoir quality has permeated published work for decades (e.g. Branner, 1937; Landes, 1967; Hayes, 1991). Deep drilling in certain geological provinces, however, has demonstrated the preservation of reservoir quality that is exceptional considering the

depth and thermal conditions to which the reservoirs have been exposed (e.g. Thomson, 1979; Dixon *et al.*, 1989; Kugler and McHugh, 1990; Law and Spencer, 1993). The Spiro sandstone qualifies as one of these exceptional reservoirs, not so much because of the depths at which exceptional reservoir quality have been encountered, but because of the levels of thermal maturity of the reservoir (Houseknecht and Spötl, 1993). The results of this study document that primary porosity can be preserved at thermal maturities that are widely regarded as indicative of tight, incipient metamorphic rocks (e.g. Landes, 1967; Hayes, 1991).

The few detailed diagenetic studies of ultra-deep and/or high thermal maturity sandstone reservoirs reveal certain common characteristics. These include evidence that relatively early, pre-hydrocarbon accumulation diagenesis influenced reservoir quality (e.g. chlorite coatings as opposed to illite cutans), that solid residues of hydrocarbons (pyrobitumen) are present, that overpressuring occurred and that late, deep burial diagenesis (post-pyrobitumen formation) commonly destroyed porosity in water-wet portions of the reservoirs while having only a minor influence on reservoir quality in hydrocarbon saturated zones (e.g. Fisher and Land, 1986; Marzano *et al.*, 1988; Dixon *et al.*, 1989; Hayes, 1991).

Our work in the Spiro sandstone, together with the results from other reservoirs cited earlier, suggest that reservoir quality, which is considered exceptional for the depths and/or thermal maturities where it occurs, is commonly preserved by the presence of included hydrocarbons. It is essential to understand reservoir diagenesis in relation to hydrocarbon accumulation before the potential for reservoir preservation at great depths and elevated thermal maturities can be fully evaluated. These observations indicate that there is no simple or universal relationship between thermal maturity and porosity 'deadlines' (i.e. economic basement).

### Conclusions

Combining petrographic, geochemical and thermal history information, the following conclusions can be drawn about the diagenetic history of the Spiro sandstone in the Red Oak field and adjacent areas.

1. Initial diagenesis of the Spiro occurred in a freshwater-dominated, coastal environment grading southward into more marine facies, with formation of Fe–clay mineral coatings and peloids, low Mg calcite cementation and local precipitation of calcian rhodochrosite and apatite.
2. During early burial the Fe–clay minerals transformed into chlorite (*Ib* chamosite). The presence of these chlorite coatings effectively inhibited quartz cementation in the porous, medium-grained sandstones.
3. Before or concomitant with hydrocarbon emplacement, pervasive ankerite precipitated in the Spiro sandstone. Ankerite formation over a range of burial depths is suggested by oxygen isotopic compositions that imply a range of minimum precipitation temperatures of 68–121°C.
4. Liquid hydrocarbons contained in the Spiro were

- thermally degraded to methane and pyrobitumen, indicating that the reservoir was heated to temperatures well in excess of  $\sim 150^{\circ}\text{C}$ .
5. Deep burial diagenetic events in the Spiro include crystallization of a high temperature chlorite generation (polytype IIb), locally extensive cementation by a non-syntaxial, pseudo-poikilotopic quartz variety uncommon in other hydrocarbon reservoirs and the precipitation of ferroan calcite and traces of (?)dickite. Independent temperature control on these high temperature processes is sparse, but available fluid inclusion data suggest temperatures in the range of  $\sim 140$  to  $\sim 220^{\circ}\text{C}$ . These temperatures approach those estimated from vitrinite reflectance values, suggesting that the late-stage inorganic diagenetic processes occurred close to or at maximum temperatures.
  6. This case study demonstrates that, despite deep burial and high temperatures — estimates based on the empirical temperature- $R_o$  relationship of Barker and Pawlewicz (1994) suggest maximum burial temperatures at the Spiro level of up to  $250^{\circ}\text{C}$  — (a) excellent porosity is preserved in the Spiro sandstone reservoir and (b) seal integrity (provided by the overlying thick Atoka mudrocks) was maintained, so that (c) commercial amounts of natural gas were preserved in this reservoir.

## Acknowledgements

This work was initiated at the University of Missouri, with partial funding by the Arkoma Basin Thermal Maturity Research Program supported by Amoco, Anadarko, Arco, Arkla, Conoco, Exxon, Maxus, Mobil, Noco, Oxy, Pennzoil, Shell, Texaco, Weyerhaeuser and Yates petroleum companies. Partial support was also provided by American Chemical Society — Petroleum Research Fund (ACS-PRF #25925-AC2). The work was completed at, and partly supported by, the US Geological Survey. Review comments by Marty Goldhaber, Neil Fishman (both US Geological Survey, Denver), Reinhard Gaupp (University of Mainz, Germany) and Journal referee J. G. Gluyas (BP Research, Sunbury-on-Thames) and an anonymous reviewer are gratefully acknowledged.

## References

- Barker, C. (1990) Calculated volume and pressure changes during the thermal cracking of oil to gas in reservoirs *Am. Assoc. Petrol. Geol. Bull.* **74**, 1254–1261
- Barker, C. E. and Pawlewicz, M. J. (1994) Calculations of vitrinite reflectance from thermal histories and peak temperature: a comparison of methods. In: *Reevaluation of Vitrinite Reflectance* (Eds P. K. Mukhopadhyay and W. G. Dow), *Am. Chem. Soc. Symp. Ser.* **570**, 216–229
- Boles, J. R. (1978) Active ankerite cementation in the subsurface Eocene of southwest Texas *Contrib. Mineral. Petrol.* **68**, 13–22
- Branan, C. B. (1968) Natural gas in Arkoma basin of Oklahoma and Arkansas. In: *Natural Gases of North America* (Ed. B. W. Beebel), *Am. Assoc. Petrol. Geol. Mem.* No. 9, 1616–1635
- Branner, G. C. (1937) Sandstone porosities in Paleozoic region in Arkansas *Am. Assoc. Petrol. Geol. Bull.* **21**, 67–79
- Cardott, B. J. (1986) Present geothermal gradient and coal rank in the Arkoma basin, Oklahoma. In: *The Relationship Between Coal Rank and Present Geothermal Gradient in the Arkoma Basin, Oklahoma* (Eds. B. J. Cardott, L. A. Hemish, C. R. Johnson and K. V. Luza) *Spec. Publ. Oklahoma Geol. Surv.* **86-4**, 27–40
- Cathles, L. M. (1993) A discussion of flow mechanisms responsible for alteration and mineralization in the Cambrian aquifers of the Ouachita–Arkoma basin–Ozark system. In: *Diagenesis and Basin Development* (Eds A. D. Horbury and A. G. Robinson), *Am. Assoc. Petrol. Geol. Stud. Geol.* **36**, 99–112
- Collins, P. L. F. (1979) Gas hydrates in CO<sub>2</sub>-bearing fluid inclusions and the use of freezing data for estimation of salinity *Econ. Geol.* **74**, 1435–1444
- Curtis, C. D., Hughes, C. R., Whiteman, J. A. and Whittle, C. K. (1985) Compositional variation within some sedimentary chlorites and some comments on their origin *Mineral. Mag.* **49**, 375–386
- Dixon, S. A., Summers, D. M. and Surdam, R. C. (1989) Diagenesis and preservation of porosity in Norphlet Formation (Upper Jurassic), southern Alabama *Am. Assoc. Petrol. Geol. Bull.* **73**, 707–728
- Dutton, S. P. and Land, L. S. (1988) Cementation and burial history of a low-permeability quartzarenite, Lower Cretaceous Travis Peak Formation, East Texas *Geol. Soc. Am. Bull.* **100**, 1271–1282
- Fisher, R. S. and Land, L. S. (1986) Diagenetic history of Eocene Wilcox sandstones, south-central Texas *Geochim. Cosmochim. Acta* **50**, 551–561
- Friedman, I. and O’Neil, J. R. (1977) Compilation of stable isotope fractionation factors of geochemical interest. In: *Data of Geochemistry* (Ed. M. Fleischer), 6th edn, *US Geol. Surv. Prof. Pap.* 440-KK, 1–12
- Ge, S. and Garven, G. (1992) Hydromechanical modeling of tectonically driven groundwater flow with application to the Arkoma foreland basin *J. Geophys. Res.* **97/B6**, 9119–9144
- Hayes, J. B. (1991) Porosity evolution of sandstones related to vitrinite reflectance *Org. Geochem.* **17**, 117–129
- Hemish, L. A. (1988) Coal geology of the lower Boggy Formation in the shelf-to-basin transition area, eastern Oklahoma. In: *Shelf-to-Basin Geology and Resources of Pennsylvanian Strata in the Arkoma Basin and Frontal Ouachita Mountains of Oklahoma* (Ed. K. S. Johnson), *Oklahoma Geol. Surv. Guidebook* **25**, 7–19
- Hillier, S. (1994) Pore-lining chlorites in siliciclastic reservoir sandstones: electron microprobe, SEM and XRD data, and implications for their origin *Clay Min.* **29**, 665–679
- Houseknecht, D. W. (1986) Evolution from passive margin to foreland basin: the Atoka Formation of the Arkoma basin, south-central U.S.A. In: *Foreland Basins* (Eds P. A. Allen and P. Homewood), *Spec. Publ. Int. Assoc. Sedimentol.* No. 8, 327–345
- Houseknecht, D. W. (1987a) The Atoka Formation of the Arkoma Basin: tectonics, sedimentology, thermal maturity, sandstone petrology *Tulsa Geol. Soc. Short Course Notes*, 72 p
- Houseknecht, D. W. (1987b) Assessing the relative importance of compaction processes and cementation to the reduction of porosity in sandstones *Am. Assoc. Petrol. Geol. Bull.* **71**, 633–642
- Houseknecht, D. W. and Hathon, L. A. (1987) Petrographic constraints on models of intergranular pressure solution in quartzose sandstones *Appl. Geochem.* **2**, 507–521
- Houseknecht, D. W. and McGilvery, T. A. (1990) Red Oak field. In: *Structural Traps II. Traps Associated with Tectonic Faulting* (Eds E. A. Beaumont and N. H. Foster), *Am. Assoc. Petrol. Geol. Treatise Petrol. Geol., Atlas of Oil and Gas Fields*, 201–225
- Houseknecht, D. W. and Ross, L. M. (1992) Clay minerals in Atokan deep-water sandstone facies, Arkoma basin: origins and influence on diagenesis and reservoir quality. In: *Origin, Diagenesis, and Petrophysics of Clay Minerals in Sandstones* (Eds D. W. Houseknecht and E. D. Pittman), *Spec. Publ. Soc. Econ. Paleontol. Mineral.* **47**, 227–240
- Houseknecht, D. W. and Spötl, C. (1993) Empirical observations regarding methane deadlines in deep basins and thrust belts. In: *The Future of Energy Gases* (Ed. D. G. Howell), *US Geol. Surv. Prof. Pap.* **1570**, 217–231
- Houseknecht, D. W. and Weesner, C. M. B. (1994) Enhanced interpretations of thermal maturity using rotational reflectance of dispersed vitrinite, overmature strata of the Arkoma basin and Ouachita thrust belt *Am. Assoc. Petrol. Geol. Annu. Convention, Denver 1994, Abstract Volume*, 175
- Houseknecht, D. W., Hathon, L. A. and McGilvery, T. A. (1992) Thermal maturity of Paleozoic strata in the Arkoma basin.

- In: *Source Rocks in the Southern Midcontinent, 1990 Symposium, Norman/OK* (Eds K. S. Johnson and B. J. Cardott), *Oklahoma Geol. Surv. Circ.* **93**, 122–132
- Houseknecht, D. W., Bensley, D. F., Hathon, L. A. and Kastens, P. H. (1993) Rotational reflectance properties of Arkoma basin dispersed vitrinite — insights for understanding reflectance populations in high thermal maturity regions *Org. Geochem.* **20**, 187–196
- Hudson, J. D. and Anderson, T. F. (1989) Ocean temperatures and isotopic compositions through time *Trans. Roy. Soc. Edinburgh: Earth Sci.* **82**, 183–192
- Jahren, J. S. and Aagaard, P. (1989) Compositional variations in diagenetic chlorites and illites, and relationships with formation-water chemistry *Clay Min.* **24**, 157–170
- Jakobsen, R. and Postma, D. (1989) Formation and solid solution behavior of Ca-rhodochrosites in marine muds of the Baltic deeps *Geochim. Cosmochim. Acta* **53**, 2639–2648
- Kantorowicz, J. D. (1985) The origin of authigenic ankerite from the Ninian field, UK North Sea *Nature* **315**, 214–216
- Kugler, R. L. and McHugh, A. (1990) Regional diagenetic variation in Norphlet sandstone: implications for reservoir quality and the origin of porosity *Gulf Coast Assoc. Geol. Soc. Trans.* **40**, 411–423
- Land, L. S. and Fisher, R. S. (1987) Wilcox sandstone diagensis, Texas Gulf Coast: a regional isotopic comparison with the Frio Formation. In: *Diagenesis of Sedimentary Sequences* (Ed. J. D. Marshall), *Spec. Publ. Geol. Soc. London No.* **36**, 219–235
- Landes, K. K. (1967) Eometamorphism, and oil and gas in time and space *Am. Assoc. Petrol. Geol. Bull.* **51**, 828–841
- Law, B. E. and Spencer, C. W. (1993) Gas in tight reservoirs — an emerging major source of energy. In: *The Future of Energy Gases* (Ed. D. G. Howell), *US Geol. Surv. Prof. Pap.* **1570**, 233–252
- Lohmann, K. C. and Walker, J. C. G. (1989) The  $\delta^{18}\text{O}$  record of Phanerozoic abiotic marine calcite cements *Geophys. Res. Lett.* **16**, 319–322
- Lumsden, D. N., Pittman, E. D. and Buchanan, R. S. (1971) Sedimentation and petrology of Spiro and Foster sands (Pennsylvanian), McAlester Basin, Oklahoma *Am. Assoc. Petrol. Geol. Bull.* **55**, 254–266
- Marzano, M. S., Pense, G. M. Andronaco, P. (1988) A comparison of the Jurassic Norphlet Formation in Mary Ann field, Mobile Bay, Alabama to onshore regional Norphlet trends *Gulf Coast Assoc. Geol. Soc. Trans.* **38**, 87–100
- McDowell, S. D. and Paces, J. B. (1985) Carbonate alteration minerals in the Salton Sea geothermal system, California, USA *Mineral. Mag.* **49**, 469–479
- North, F. K. (1985) *Petroleum Geology*, Unwin Hyman, Boston, 631 pp
- Odin, G. S. (1988) *Green Marine Clays, Dev. Sedimentol.* **45**, Amsterdam, Elsevier, 445 pp
- Odin, G. S. (1990) Clay mineral formation at the continent-ocean boundary: the verdine facies *Clay Min.* **25**, 477–483
- Pittman, E. D. and Lumsden, D. N. (1968) Relationship between chlorite coatings on quartz grains and porosity, Spiro sand, Oklahoma *J. Sedim. Petrol.* **38**, 668–670
- Pittman, E. D., Larese, R. E. and Heald, M. T. (1992) Clay coats: occurrence and relevance to preservation of porosity in sandstones. In: *Origin, Diagenesis and Petrophysics of Clay Minerals in Sandstones* (Eds D. W. Houseknecht and E. D. Pittman), *Spec. Publ. Soc. Econ. Paleontol. Mineral. No.* **47**, 241–255
- Porrenga, D. H. (1966) Clay minerals in recent sediments of the Niger delta *Clays Clay Min.* **26**, 221–233
- Powell, T. G. and Snowdon, L. R. (1983) A composite hydrocarbon generation model. Implications for evaluation of basins for oil and gas *Erdöl Kohle Erdgas Petrochem.* **36**, 163–170
- Prezbindowski, D. R. and Tapp, J. B. (1991) Dynamics of fluid inclusion alteration in sedimentary rocks: a review and discussion *Org. Geochem.* **17**, 131–142
- Ramseyer, K. and Mullis, J. (1990) Factors influencing short-lived blue cathodoluminescence of alpha-quartz *Am. Mineral.* **75**, 791–800
- Roedder, E. (1984) *Fluid Inclusions, Rev. Mineral.* **12**, American Mineralogical Society, Washington, 646 pp
- Spötl, C., Houseknecht, D. W. and Jaques, R. (1993) Clay mineralogy and illite crystallinity of the Atoka Formation, Arkoma basin, and frontal Ouachita Mountains *Clays Clay Min.* **41**, 745–754
- Spötl, C., Houseknecht, D. W. and Longstaffe, F. J. (1994) Authigenic chlorites in sandstones as indicators of high-temperature diagenesis, Arkoma foreland basin, U.S.A. *J. Sedim. Res.* **A64**, 553–566
- Suchecki, R. K. and Land, L. S. (1983) Isotopic geochemistry of burial-metamorphosed volcanogenic sediments, Great Valley sequence, northern California *Geochim. Cosmochim. Acta* **47**, 1487–1499
- Thomson, A. (1979) Preservation of porosity in the deep Woodbine/Tuscaloosa trend, Louisiana *Gulf Coast Assoc. Geol. Soc. Trans.* **29**, 396–403
- Tissot, B. P. and Welte, D. H. (1984) *Petroleum Formation and Occurrence*, Springer, New York, 699 pp
- Werner, W. G. and Griffith, C. E. (1992) The Arkoma basin — an overmature gas province *Am. Assoc. Petrol. Geol. Annu. Convention, Calgary 1992, Abstract Volume*, 140
- Wilkinson, M., Crowley, S. F. and Marshall, J. D. (1992) Model for the evolution of oxygen isotope ratios in the pore fluids of mudrocks during burial *Mar. Petrol. Geol.* **9**, 98–105
- Wojcik, K. M., McKibben, M. E., Goldstein, R. H. and Walton, A. W. (1992) Diagenesis, thermal history, and fluid migration, Middle and Upper Pennsylvanian rocks, southeastern Kansas. In: *Source Rocks in the Southern Midcontinent, 1990 Symposium, Norman/OK* (Eds K. S. Johnson and B. J. Cardott) *Oklahoma Geol. Surv. Circ.* **93**, 144–159
- Wojcik, K. M., Goldstein, R. H. and Walton, A. W. (1994) History of diagenetic fluids in a distant foreland area, Middle and Upper Pennsylvanian, Cherokee basin, Kansas, USA: fluid inclusion evidence *Geochim. Cosmochim. Acta* **58**, 1175–1191